

Anisotropic inversion of seismic data for stressed media: Theory and a physical modeling study on Berea Sandstone

Debashish Sarkar*, Andrey Bakulin†, and Robert L. Kranz*

ABSTRACT

Nonhydrostatic stress, an often-ignored source of seismic anisotropy, is universally present in the subsurface and may be as common as intrinsic or fracture-induced anisotropy. Nonhydrostatic stress, applied to an initially transversely isotropic solid with vertical symmetry axis (VTI), results in an effective medium having almost orthorhombic symmetry (provided that one of the principal stresses is aligned with the symmetry axis). The symmetry planes observed in this orthorhombic medium are aligned with the orientations of the principal stresses, and anisotropic parameters ($\epsilon^{(1,2)}$, $\delta^{(1,2,3)}$, and $\gamma^{(1,2)}$) can reveal information about the stress magnitudes. Thus, time-lapse monitoring of changes in anisotropy potentially can provide information on temporal variations in the stress field.

We use nonlinear elasticity theory to relate the anisotropic parameters to the magnitudes of the principal stresses and verify these relationships in a physical modeling study. Under the assumption of weak background and stress-induced anisotropy, each effective anisotropic parameter reduces to the sum of the corresponding Thomsen parameter for the unstressed VTI background and the corresponding parameter associated with the nonhydrostatic stress. The stress-related anisotropic parameters depend only on the differences between the magnitudes of principal stresses; therefore,

principal stresses can influence anisotropic parameters only if their magnitudes differ in the symmetry plane in which the anisotropic parameters are defined.

We test these predictions on a physical modeling data set acquired on a block of Berea Sandstone exhibiting intrinsic VTI anisotropy. Uniaxial stress, applied normal to the VTI symmetry axis, i.e., horizontally, produces an effective medium that is close to orthorhombic. We use two different methods to estimate the anisotropic parameters and study their variation as a function of stress. The first method utilizes conventional measurements of transmission velocities along the principal axes of the sample. The second method uses PP and PS reflection data acquired along seven different azimuths on the surface of the block.

In accordance with theoretical predictions, the anisotropic parameters in the vertical plane normal to the stress are almost insensitive to the magnitude of the stress. In contrast, anisotropic parameters in the vertical plane of the applied stress increase approximately in a linear fashion with increasing stress. Except for the parameter $\delta^{(1)}$, comparison of the measured values of anisotropic parameters with theoretical predictions shows satisfactory agreement.

Despite some documented discrepancies, we believe that nonlinear elasticity may provide a suitable framework for estimating pore pressure and 3D stresses from seismic data.

INTRODUCTION

Estimating and monitoring subsurface stress levels is important for a variety of reasons:

- 1) knowledge of the current stress field is crucial for planning drilling and mining operations and for resolving wellbore and mine stability problems;

- 2) tectonic stresses, past and present, determine fracture patterns, which in turn control the movement of fluids;
- 3) pore pressure and 3D stress monitoring during recovery of hydrocarbons provides valuable input for optimizing reservoir depletion strategy and reducing the risk of various hazards, e.g., well blowouts caused by fluid overpressure; and

Published on Geophysics Online November 26, 2002. Manuscript received by the Editor January 18, 2002; revised manuscript received August 21, 2002.

*Colorado School of Mines, Department of Geophysics, Golden, Colorado 80401-1887. E-mail: dsarkar@mines.edu; rlk37@aol.com.

†Formerly Schlumberger Cambridge Research, High Cross, Madingley Road, Cambridge, CB3 0EL, England; presently Shell International Exploration and Production, Post Office Box 481, Houston, Texas 77001-0481. E-mail: andrey.bakulin@shell.com.

© 2003 Society of Exploration Geophysicists. All rights reserved.

- 4) pore pressure and 3D stress influence the velocities of seismic waves; therefore, in time-lapse seismic measurements, their contribution must be removed before monitoring changes in fluid distribution inside reservoirs.

The presence of initial stress influences the dynamic response of a medium; therefore, monitoring changes in elastic properties and anisotropy provides a way of monitoring stress levels. This phenomenon is similar to the change in the velocity of transverse vibrations along a string when the tension of the string is changed. Various methods of estimating pore pressure used in the oil industry utilize this principle to obtain 3D pore-pressure fields (Eaton, 1975; Bowers, 1995). These methods, however, are based on empirical relationships between seismic velocity and effective hydrostatic stress (often approximated as the difference between lithostatic stress and pore pressure) and rely on several assumptions that are often unrealistic for the subsurface. Two issues impair their applicability:

- 1) subsurface stresses are nonhydrostatic (Fjær et al., 1992); the three principal stresses are, in general, unequal, and their orientations and magnitudes should be recovered to obtain a realistic description of the 3D stress field; and
- 2) subsurface formations are not isotropic; they possess both intrinsic and stress-induced anisotropy.

Of the two issues, the latter may be addressed by multi-component seismic methods, which allow for estimating the anisotropic velocity field or stiffness tensor (Grechka et al., 2002).

Addressing the first problem is more challenging because it requires sound theory that goes beyond the simplistic 1D, P-wave-only empirical models typically used in practice (Eaton, 1975; Bowers, 1995). Here, to address this problem, we propose to use nonlinear elasticity (Thurston and Brugger, 1964; Thurston, 1974) as a theoretical basis for studying stress-induced anisotropy, because this theory gives a full mapping between the arbitrary triaxial stress field and the anisotropic stiffness tensor, accounts for intrinsic anisotropy of the unstressed rock, and requires only three constants of nonlinear elasticity (stress-sensitivity parameters) to describe stress-dependent velocities for all wave modes in all directions.

Prioul et al. (2001) show that nonlinear elasticity can describe the properties of intrinsically anisotropic shales and sands as a function of stress. Indeed, nonlinear elasticity theory provides a rigorous link between stresses and the effective stiffness tensor. For example, it supports the intuitive expectation that an isotropic solid in the presence of uniaxial stress exhibits symmetry close to hexagonal, while a transversely isotropic solid, in the presence of uniaxial stress in the isotropy plane, exhibits anisotropy close to orthorhombic.

Previously, it was difficult to relate laboratory measurements to field observations because in-situ estimates of the nonlinear constants were unavailable. This is one reason why this theory has lacked widespread acceptance. However, today, estimates of nonlinear constants are available not only from lab measurements on cores but also from in-situ multimode borehole acoustics (Sinha and Winkler, 1999; Sinha et al., 2000; Sinha, 2001). This makes downhole calibration of nonlinear constants possible.

Most experimental studies have focused on measurements of stress-induced velocity anisotropy in rocks that are isotropic

in the absence of stress (e.g., Nur, 1971; Mavko et al., 1995; Johnson and Rasolofosaon, 1996). However, rocks can exhibit significant anisotropy even in the absence of stress (e.g., Tsvankin, 2001). It is therefore of interest to study how stresses change velocity anisotropy of a rock that is already anisotropic in the unstressed state. Lo et al. (1986) and Hornby (1998) have performed such a study on transversely isotropic (TI) rocks, but their data are limited to experiments where all principal stresses are equal. In most subsurface conditions, however, principal stresses differ significantly (Fjær et al., 1992). Typically the magnitude of the vertical stress exceeds that of the horizontal stress, but such a situation may be reversed in active tectonic regions (e.g., those with thrust faulting), where horizontal stresses can be more than twice as large as the vertical stress (Bourgoyne et al., 1991). In addition, the horizontal stresses may vary with azimuth.

To study the influence of nonhydrostatic stress on anisotropy, we applied uniaxial load to an initially TI rock (Berea Sandstone) and monitored the change in velocity anisotropy with stress. We applied three levels of stress—3, 6, and 9 MPa (9 MPa is about one-tenth the burial pressure of Berea Sandstone of Mississippian age or about one-fourth its uniaxial fracture strength)—along the isotropy plane to create velocity anisotropy that has a symmetry close to orthorhombic. We then related the observed anisotropic parameters to the stress level using a nonlinear elasticity theory and, in the limit of weak anisotropy, obtained insight into the effect of stress on anisotropy.

EXPERIMENTAL SETUP AND INSTRUMENTATION

We used a block of buff-colored Berea sandstone (304 × 304 × 152 mm from the Cleveland quarry near Amherst, Ohio, USA) for our experiment. The bulk density of the rock was 2.14 g/cm³ by bulk weight. Since the dominant material in Berea sandstone is quartz, with silicic cement and almost no clay, this density implies a porosity of about 21%. The average grain size was 150–250 μ. The block appeared homogeneous at the centimeter scale and above. Some bedding was observed perpendicular to the x_3 -axis direction (Figures 1 and 2), and no cross-bedding was visible.

Berea sandstone is known to be anisotropic (e.g., Thomsen, 1986; Lo et al., 1986). The anisotropy comes primarily from the weak preference for prismatic quartz grains to lie in the bedding planes and to have elongated, microcrack-like contacts between grains. Some pore-space elongation is evident perpendicular to bedding planes but not in the bedding planes (Prasad and Manghnani, 1997).

For the transmission measurements in the directions of x_1 - and x_2 -axes, two pairs of aluminum side plates (304 × 152 × 25.34 mm) were fabricated with three wells (22.17 mm diameter and 9.5 mm deep) placed near the plate midpoints (Figures 1 and 2). Three piezoelectric transducers, one compressional and two carefully oriented shear disks, were epoxied in the wells, and electrical leads were taken out through the plates. A pair of aluminum plates was glued to opposing [x_2, x_3] faces of the block while the other pair was glued to the opposing [x_1, x_3] faces. They were oriented so that transducers of the same polarization were directly opposite each other.

The two pairs of matched plates were calibrated to determine the inherent (zero-length) delay times for P- and S-wave

propagation into the rock. The calibrations for both sets of matched plates were almost identical, yielding delay times of 0.37 and 0.43 μs for P-wave and 0.84 and 0.90 μs for S-wave traveltimes. These times represent $<1\%$ of the total traveltimes and were ignored. For measurements in the x_3 -axis direction, we used hand-held individual Ultrason transducers to obtain velocities of the different wave modes.

Reflection surveys were conducted with the source and receiver transducers on the same unstressed block surface represented by the $[x_1, x_2]$ plane (Figures 1 and 2). A compressional Panametrics transducer providing the impulsive source was epoxied to the block about 5 cm from the lower-left corner. We used hand-held Ultrason compressional and shear receiver transducers pressed against the rock surface with an

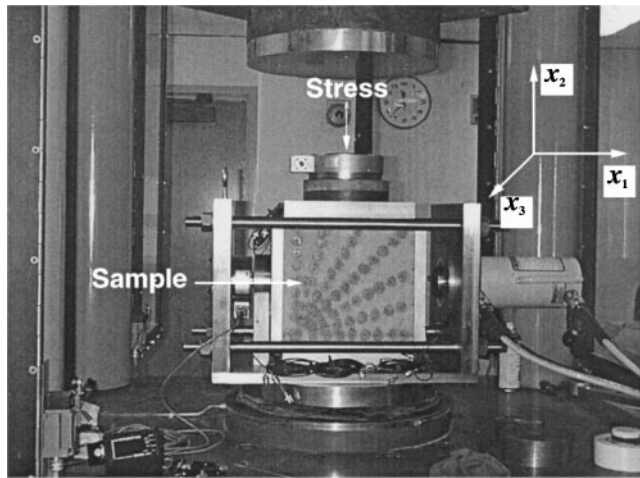


FIG. 1. Photograph of the actual experimental set-up. The marks on the sample indicate transducer positions for the reflection measurements. The bedding plane of the rock is aligned in the $[x_1, x_2]$ plane. The block of rock has been oriented so that the loading is parallel to the bedding plane. In this picture the axis of the VTI medium is pointing toward the viewer.

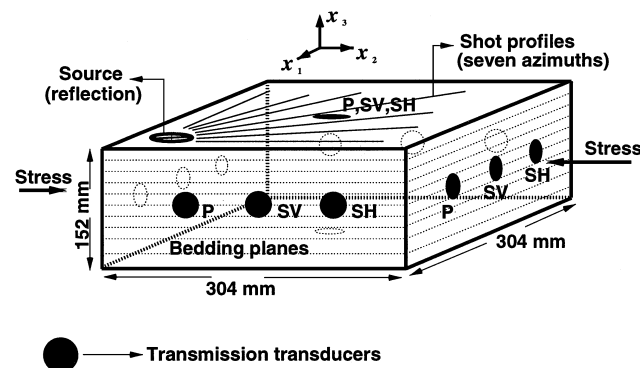


FIG. 2. Schematic of the performed experiment. The sample of Berea Sandstone has been restored to its original in-situ orientation. Bedding planes are drawn schematically. Reference in the text to top and bottom refer to this (in-situ) orientation. Transmission velocities were measured by transducers (shown here as solid circles) placed in the middle of each face. Multi-azimuth acquisition of PP and PS reflection data was conducted on the top (i.e., $[x_1, x_2]$ plane) of the block. In this orientation the axis of the VTI medium is pointing vertically, parallel to the x_3 -axis.

intervening, molasses-based couplant. Seven 2D lines were acquired along azimuths at $0^\circ, 15^\circ, 30^\circ, 45^\circ, 60^\circ, 75^\circ,$ and 90° measured counterclockwise from the x_1 -axis direction. For all azimuths, minimum source–receiver offset was 4 cm, and adjacent receiver positions were spaced 3 cm apart. Along each azimuth separate reflection surveys were conducted consecutively with compressional receivers, in-line shear (polarized along the direction of the line) receivers, and cross-line shear receivers (polarized perpendicular to the line).

To enhance S/N amplitude ratio, we stacked 512 repetitions of received waveform signals (both transmission and reflection) before stopping the digitization. To generate source pulses, we used a portable pulser with a fixed excitation source pulse of approximately 400 V and 3 μs width for all transmission and reflection measurements. Stresses were applied to the sandstone block in the x_2 -axis direction through the aluminum side plates using a 1 000 000-lb servo-controlled hydraulic press from the Colorado School of Mines (CSM) Mining Department.

DATA PROCESSING

We processed the recorded waveforms by applying only a time-variant gain to compensate for geometrical spreading and a spiking deconvolution to improve temporal resolution. Ambient vibrations in the experimental equipment were transmitted to the rock and were picked up by the receiving transducers as unwanted noise. We removed the noise with a 60-100-800-1000-kHz trapezoidal bandpass filter.

The P-wave reflected from the bottom face of the block and the converted PSV-wave were the main phases in all in-line gathers. Some lines also contained pure-shear reflections on the cross-line components. For each event and each azimuth, we estimated NMO velocity from semblance analysis. Since NMO velocity describes traveltimes accurately for near offsets, we used only the first five traces, or a maximum offset-to-depth ratio of about one, in the semblance analysis.

The semblance measure used here is defined as (Taner and Koehler, 1969)

$$S(v, t_0) \equiv \frac{\sum_{t_1} [\sum_x D_v(t_1, x)]^2}{N \sum_{t_1} \sum_x D_v^2(t_1, x)}, \quad (1)$$

where $D_v(t_1, x) = D[t_v(t_1, x), x]$, with $t_v(t_1, x) = \sqrt{t_1^2 + x^2/v^2}$; t_1 are zero-offset times within a window centered at t_0 ; x is source–receiver offset; and $N = 5$ is the number of traces in a shot gather. The value D_v represents the moveout-corrected data with trial moveout velocity v , and D represents the data without NMO correction. At each zero-offset time t_0 , we computed the semblance measure for different values of v and chose the value of v that maximized the semblance measure as the desired NMO velocity, V_{nmo} .

For transmission velocity measurements in the unstressed rock, we estimated the traveltime of P-waves by manually picking the first break, which was always sharp and clear. For the traveltime of S-waves, however, we manually estimated the onset of the main S-wave energy. At higher stress states, traveltime lags were computed by crosscorrelating the waveforms obtained in the stressed states with those obtained in the unstressed state. We then estimated traveltimes of the different modes by adding this traveltime lag to the traveltimes picked in the unstressed state.

MEASUREMENTS OF TRANSMISSION VELOCITIES OF PURE MODES

Table 1 shows transmission velocities in the stressed and unstressed states recorded in the coordinate directions x_1 , x_2 , and x_3 . The first subscript for S-waves refers to the direction of propagation; the second subscript refers to the polarization direction. The subscript for P-waves indicates the direction of propagation. The listed errors in velocity correspond to an assumed ± 1 - μ s error in traveltimes in the x_1 and x_2 directions and ± 0.5 μ s in the x_3 direction. This corresponds to an error of less than ± 0.02 km/s in velocity. We chose a conservative estimate of ± 0.02 km/s for our error in all our transmission velocity measurements. As has been observed in other experiments (Lo et al., 1986), our unstressed Berea Sandstone is also transversely isotropic with $V_{S31} = V_{S13} = V_{S32} = V_{S23}$ and $V_{P1} = V_{P2}$. This means that our $[x_1, x_2]$ -plane is a plane of isotropy, and the x_3 -axis is the axis of symmetry, i.e., the medium is transversely isotropic with a vertical symmetry axis (VTI).

When we increase the stress level in the x_2 -axis direction, the P-wave velocity (V_{P2}) in this direction also increases. However, the velocity of P-waves propagating perpendicular to the stress field (V_{P1} , V_{P3}) remains almost unchanged. The velocities of S-waves (e.g., V_{S23} , V_{S32}) propagating in the direction of the applied stress or having a displacement component in that direction also increase with the stress level. In contrast, the velocities of S-waves propagating perpendicular to the direction of applied stress and polarized perpendicular to the applied stress (V_{S13} , V_{S31}) remain unaltered by changes in the stress level. We attribute the large changes in V_{P2} , V_{S23} , and V_{S32} to the preferential opening and closing of cracks. Also note the stress-induced asymmetry in the velocities ($V_{Sij} \neq V_{Sji}$) for shear waves either propagating in the direction of the applied stress or having a displacement component in that direction, while velocities of shear waves propagating perpendicular to the direction of the applied stress and polarized perpendicular to the applied stress are symmetric within the error bars.

MEASUREMENT AND ESTIMATION OF ANISOTROPIC PARAMETERS

From the symmetry of the applied stresses and the unstressed sample, we expect the stressed sample to exhibit symmetry close to orthorhombic, with symmetry planes $[x_1, x_2]$, $[x_2, x_3]$, and $[x_1, x_3]$. Following Grechka et al. (1999), we compare two different methods for estimating the anisotropic parameters of an orthorhombic solid. Instead of the stiffness matrix [equation (A-1) in the appendix], we use another parameterization introduced by Tsvankin (1997) for orthorhombic media. His notation contains the vertical P-wave velocity and one of the velocities of vertical S-wave propagation, along with the seven dimensionless Thomsen-type (1986) anisotropic parameters described in the appendix. For an isotropic medium, all

seven anisotropic parameters vanish. For a VTI medium, only five of the nine parameters are independent. Tsvankin's parameterization is especially advantageous for seismic moveout inversion because it provides a simple, concise description of NMO velocities of all pure modes. The two methods of Grechka et al. (1999) use different combinations of transmission and NMO velocities.

Method 1

Method 1 uses the vertical and horizontal velocities of P- and S-waves along with the NMO velocities of P-waves. The relevant equations are (Grechka et al., 1999)

$$\epsilon^{(1)} = \frac{1}{2} \left(\frac{V_{P2}^2}{V_{P3}^2} - 1 \right), \quad \epsilon^{(2)} = \frac{1}{2} \left(\frac{V_{P1}^2}{V_{P3}^2} - 1 \right), \quad (2)$$

$$\gamma^{(1)} = \frac{1}{2} \left(\frac{V_{S21}^2}{V_{S31}^2} - 1 \right), \quad \gamma^{(2)} = \frac{1}{2} \left(\frac{V_{S12}^2}{V_{S32}^2} - 1 \right), \quad (3)$$

$$\delta^{(i)} = \frac{1}{2} \left(\left[\frac{V_{P,nmo}^{(i)}}{V_{P3}} \right]^2 - 1 \right), \quad (i = 1, 2). \quad (4)$$

Here and below, the superscript 1 corresponds to the $[x_2, x_3]$ plane and 2 corresponds to the $[x_1, x_3]$ plane (the superscripts denote the axis normal to each plane); $V_{P,nmo}^{(1)}$ and $V_{P,nmo}^{(2)}$ are the P-wave NMO velocities in the vertical symmetry planes $[x_2, x_3]$ and $[x_1, x_3]$, respectively.

Method 2

Method 2 uses the NMO and vertical velocities of the P- and S-waves. The relevant equations are (Grechka et al., 1999)

$$\delta^{(i)} = \frac{1}{2} \left(\left[\frac{V_{P,nmo}^{(i)}}{V_{P3}} \right]^2 - 1 \right), \quad (i = 1, 2), \quad (5)$$

$$\sigma^{(1)} = \frac{1}{2} \left(\left[\frac{V_{SV,nmo}^{(1)}}{V_{S32}} \right]^2 - 1 \right),$$

$$\sigma^{(2)} = \frac{1}{2} \left(\left[\frac{V_{SV,nmo}^{(2)}}{V_{S31}} \right]^2 - 1 \right), \quad (6)$$

$$\gamma^{(1)} = \frac{1}{2} \left(\left[\frac{V_{SH,nmo}^{(1)}}{V_{S31}} \right]^2 - 1 \right),$$

$$\gamma^{(2)} = \frac{1}{2} \left(\left[\frac{V_{SH,nmo}^{(2)}}{V_{S32}} \right]^2 - 1 \right), \quad (7)$$

$$\epsilon^{(1)} = \left(\frac{V_{S32}}{V_{P3}} \right)^2 \sigma^{(1)} + \delta^{(1)}, \quad \epsilon^{(2)} = \left(\frac{V_{S31}}{V_{P3}} \right)^2 \sigma^{(2)} + \delta^{(2)}. \quad (8)$$

Table 1. Transmission velocities along the x_1 -, x_2 -, and x_3 -axes measured at various stress levels applied in the x_2 -direction.

Stress (MPa)	V_{P1} (km/s)	V_{S13} (km/s)	V_{S12} (km/s)	V_{P2} (km/s)	V_{S23} (km/s)	V_{S21} (km/s)	V_{P3} (km/s)	V_{S32} (km/s)	V_{S31} (km/s)
0	2.45 \pm 0.02	1.63 \pm 0.02	1.77 \pm 0.02	2.45 \pm 0.02	1.63 \pm 0.02	1.76 \pm 0.02	2.30 \pm 0.02	1.64 \pm 0.02	1.62 \pm 0.02
3	2.36 \pm 0.02	1.61 \pm 0.02	1.82 \pm 0.02	2.79 \pm 0.02	1.75 \pm 0.02	1.88 \pm 0.02	2.30 \pm 0.02	1.74 \pm 0.02	1.61 \pm 0.02
6	2.36 \pm 0.02	1.65 \pm 0.02	1.90 \pm 0.02	3.04 \pm 0.02	1.85 \pm 0.02	1.98 \pm 0.02	2.33 \pm 0.02	1.82 \pm 0.02	1.64 \pm 0.02
9	2.37 \pm 0.02	1.63 \pm 0.02	1.96 \pm 0.02	3.20 \pm 0.02	1.91 \pm 0.02	2.06 \pm 0.02	2.34 \pm 0.02	1.87 \pm 0.02	1.64 \pm 0.02

Here, SV refers to shear waves propagating in the direction contained in a symmetry plane and polarized in that plane; SH refers to shear waves propagating in a symmetry plane but polarized perpendicular to the symmetry plane.

Since pure S-phases were not easy to distinguish from other events on our in-line gather, we computed the shear-wave NMO velocity—required to compute parameters $\sigma^{(i)}$ [equations (6)]—from the PP and PS converted-wave NMO velocities using the Dix-type equation (Grechka et al., 1999; Tsvankin, 2001):

$$t_0^{(PS)} [V_{PS,nmo}^{(i)}]^2 = t_0^{(P)} [V_{P,nmo}^{(i)}]^2 + t_0^{(S)} [V_{S,nmo}^{(i)}]^2, \quad (i = 1, 2), \quad (9)$$

where $t_0^{(PS)} \equiv t_0^{(P)} + t_0^{(S)}$ is the two-way zero-offset time of the PS converted wave, which is the sum of the one-way zero-offset time of P-waves ($t_0^{(P)}$) and S-waves ($t_0^{(S)}$).

For a homogeneous orthorhombic medium, NMO velocity as a function of azimuth is fully determined by the NMO velocities in the symmetry planes. The governing relationship is the equation of the NMO ellipse (Grechka et al., 1999):

$$\frac{1}{V_{Q,nmo}^2(\alpha)} = \frac{\cos^2 \alpha}{[V_{Q,nmo}^{(1)}]^2} + \frac{\sin^2 \alpha}{[V_{Q,nmo}^{(2)}]^2}, \quad (10)$$

$(Q = P, SV, \text{ or } SH),$

where the angle α represents the azimuthal direction in the $[x_1, x_2]$ -plane measured counterclockwise from the x_1 -direction.

Assuming that $[x_1, x_3]$ and $[x_2, x_3]$ are the two vertical planes of symmetry of the stressed sample, we computed

anisotropic parameters for different levels of stress. The NMO velocities and corresponding moveout curves used to compute the parameters are shown superimposed on the shot gathers in Figures 3–7. Since the pure-shear event (Figure 7) is not observed in the cross-line shot gathers along the x_2 -direction, $\gamma^{(1)}$ is not computed using method 2 and the cross-line gathers are not shown.

Anisotropic parameters of the effective orthorhombic medium

Table 2 shows the anisotropic parameters estimated using methods 1 and 2 at various stress levels. For the unstressed experiment, both methods produce similar estimates, while the estimates of the parameters differ between the methods at higher stress states. The tables suggest that anisotropic parameters defined in the $[x_2, x_3]$ plane (the plane parallel to the stress direction) are in general larger and more sensitive to the applied stress than those defined in the $[x_1, x_3]$ plane (the plane perpendicular to the stress direction).

Figure 8 shows NMO velocities of P- and PSV-waves measured in the unstressed state as a function of azimuth. The NMO ellipses were computed as a least-squares fit to the measured values. The pure-shear wave (SV) NMO ellipse computed using equation (9) is also shown in Figure 8. All three ellipses are close to being concentric circles, which confirms that the model is VTI, that the x_3 -axis (the vertical direction) is the axis of symmetry, and that $[x_1, x_2]$ is the isotropy plane.

Figure 9 shows the P-wave NMO ellipses for different stress states computed using a least-squares fit to the NMO velocities and assuming that $[x_1, x_3]$ and $[x_2, x_3]$ are the vertical planes of symmetry of the stressed sample. The difference between the major and minor axes of the different ellipses increases with stress level. We did not produce NMO ellipses for converted

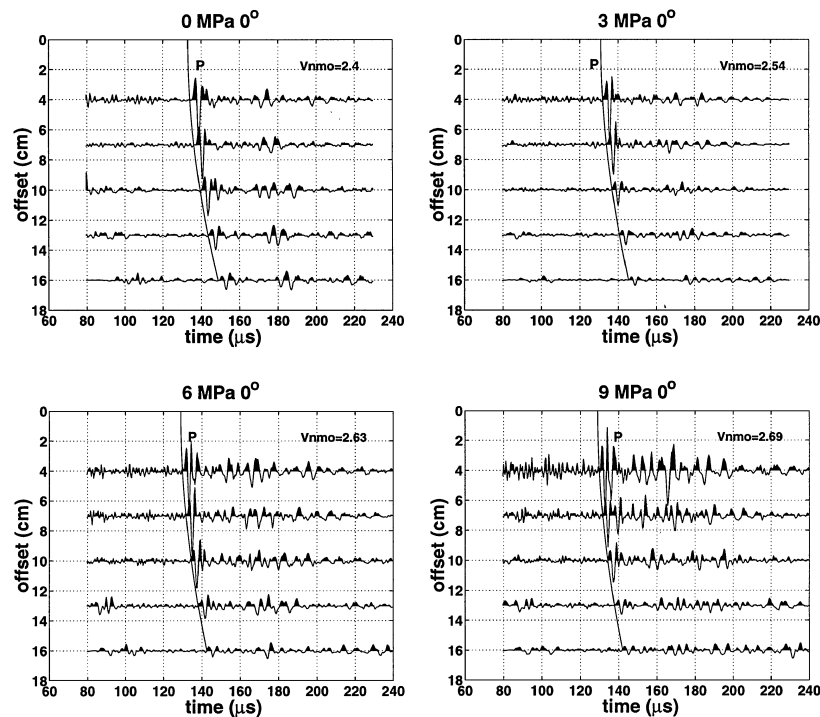


FIG. 3. Seimograms of the vertical displacement component recorded at azimuth 0° (in the x_1 -axis direction or perpendicular to the applied stress) at different stress levels. The most prominent arrival is the P-wave reflection from the bottom of the block. In Figures 3–7 velocity is measured in kilometers per second, and the curves represent the estimated moveout with the moveout velocity shown alongside.

waves at higher stress states because we were unable to identify each split converted-wave mode at intermediate azimuths (15° – 75°) and therefore were unable to estimate their NMO velocities accurately.

NONLINEAR ELASTICITY THEORY

We compared predictions made from nonlinear elasticity theory (Thurston and Brugger, 1964; Thurston, 1974; Bakulin et al., 2000d) with the measured data. Configurations **A**, **B**,

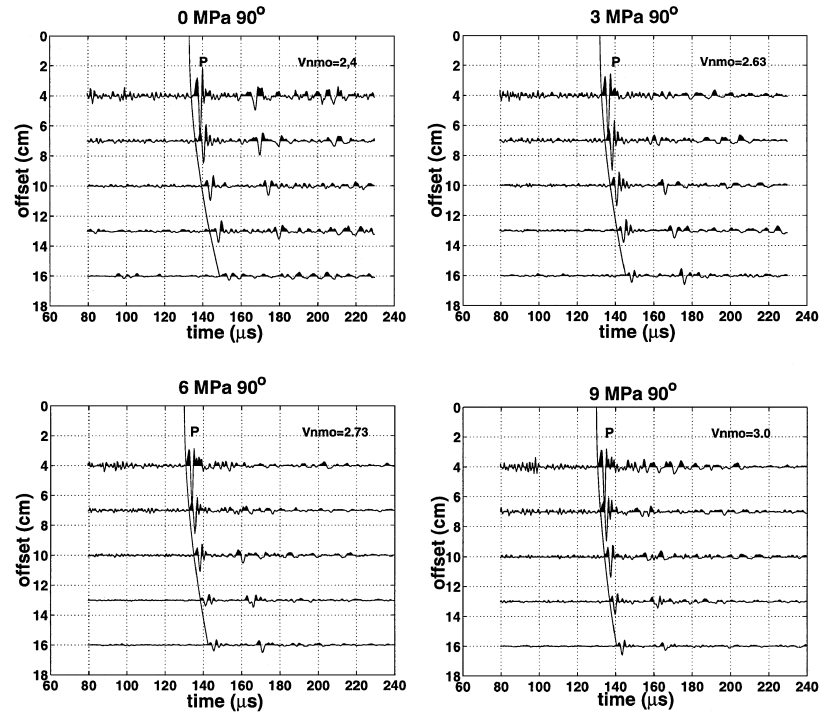


FIG. 4. Same as in Figure 3, but now for azimuth 90° (in the x_2 -axis direction or parallel to the applied stress).

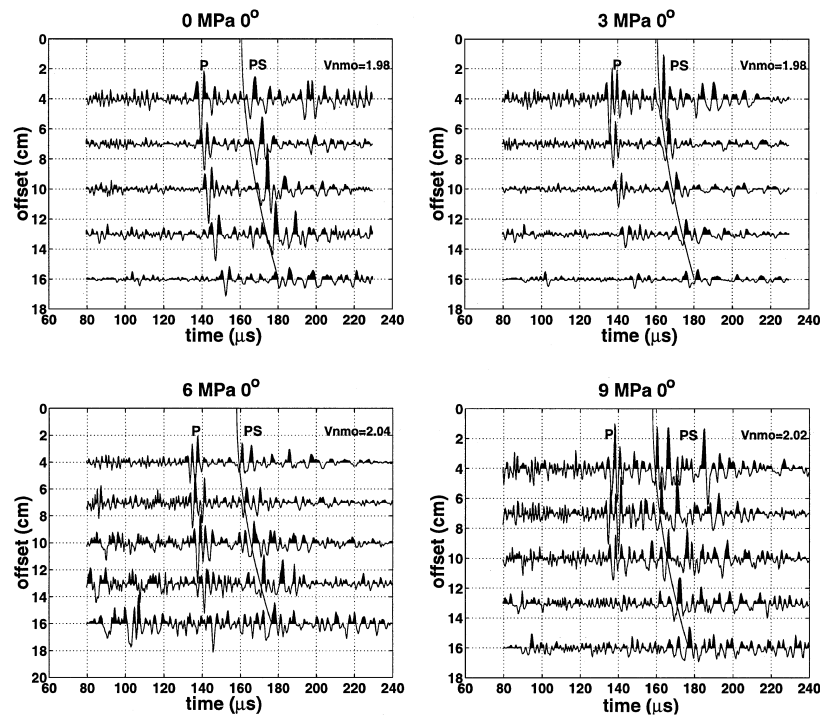


FIG. 5. Seismograms of the in-line horizontal component recorded at azimuth 0° (in the x_1 -axis direction or perpendicular to the applied stress) at different stress levels. The most prominent arrival is the converted-wave PSV reflection from the bottom of the block.

and **C** (Figure 10) refer to the unstressed state, deformed state, and wave-propagation state, respectively, and are portrayed in a Cartesian coordinate frame (x_1, x_2, x_3) .

State **A** is the stress-free state of the medium; the stiffness tensor in this state is referred to as A_{ijpq} . After application of stress τ_{ij} , the medium deforms to a new state **B**; B_{ijpq} refers

to the stiffness tensor that describes static deformations about this deformed state. The stiffness tensors in states **A** and **B** are related through the deformation gradient tensor [such as $\partial b_i / \partial a_i$, in equation (11)] that describes the change from **A** to **B**.

When small-amplitude waves such as those encountered in typical seismic experiments propagate through this stressed

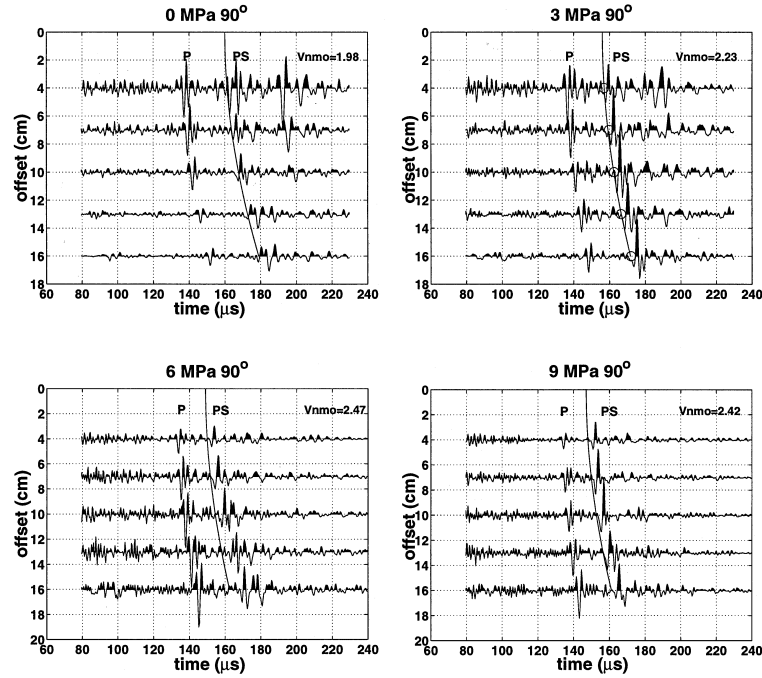


FIG. 6. Same as in Figure 5, but now for azimuth 90° (in the x_2 -axis direction or parallel to the applied stress).

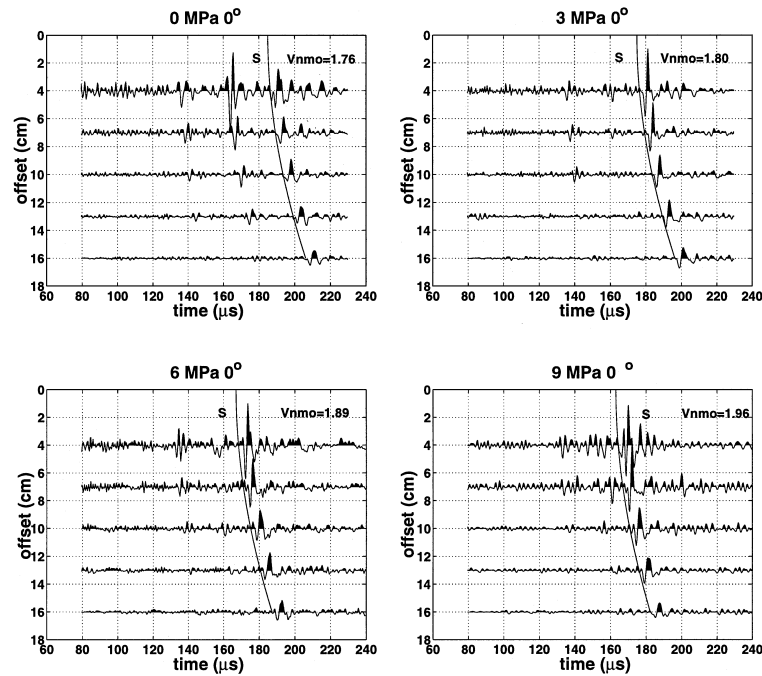


FIG. 7. Processed seismograms of the cross-line horizontal component recorded at azimuth 0° (in the x_1 -axis direction or perpendicular to the applied stress). The most prominent arrival is the SH-SH reflection from the bottom of the block. Theory does not predict such a reflection for a point vertical force. It is likely to be caused here by a distributed surface source and imperfect block boundaries.

medium, the deformation is described as a linear change from state \mathbf{B} to a new state \mathbf{C} . The elastic coefficients that describe wave propagation in a stressed medium can be represented as an effective stiffness tensor C_{ijpq} . Since the deformation from state \mathbf{A} to state \mathbf{B} may include finite strains, nonlinear elasticity is required to describe this change. Therefore, in addition to the fourth-order stiffness tensors (A_{ijpq} and B_{ijpq}) of linear elasticity, sixth-order tensors (A_{ijpqrs} and B_{ijpqrs}) are required to describe nonlinear deformation. Here,

$$B_{ijpq} = A_{tuvw} \frac{\partial b_i}{\partial a_t} \frac{\partial b_j}{\partial a_u} \frac{\partial b_p}{\partial a_v} \frac{\partial b_q}{\partial a_w} \frac{\rho^{\mathbf{B}}}{\rho^{\mathbf{A}}}$$

and

$$B_{ijpqrs} = A_{tuvwrs} \frac{\partial b_i}{\partial a_t} \frac{\partial b_j}{\partial a_u} \frac{\partial b_p}{\partial a_v} \frac{\partial b_q}{\partial a_w} \frac{\rho^{\mathbf{B}}}{\rho^{\mathbf{A}}},$$

where b_i and a_i are components of position vectors of a particle in the stressed and unstressed states (Figure 10) and $\rho^{\mathbf{B}}$ and $\rho^{\mathbf{A}}$ are the densities in the stressed and unstressed states.

The tensors C_{ijpq} and A_{ijpq} are related (Thurston, 1974) as

$$C_{ijpq} = \delta_{ip} \tau_{jq} + (A_{tuvw} + A_{tuvwrs} \epsilon_{rs}) \frac{\partial b_i}{\partial a_t} \frac{\partial b_j}{\partial a_u} \frac{\partial b_p}{\partial a_v} \frac{\partial b_q}{\partial a_w} \frac{\rho^{\mathbf{B}}}{\rho^{\mathbf{A}}}, \quad (11)$$

where τ_{jq} is the preexisting stress field and ϵ_{rs} is the strain tensor describing the transformation from \mathbf{A} to \mathbf{B} . Strains of the order of 10^{-4} were observed in this experiment. This value is small enough to suggest that the position vectors a and b and densities $\rho^{\mathbf{A}}$ and $\rho^{\mathbf{B}}$ are approximately equal. The deformation-gradient tensor then reduces approximately to the Kronecker delta δ_{ip} , and equation (11) simplifies to

$$C_{ijpq} = \delta_{ip} \tau_{jq} + A_{ijpq} + A_{ijpqrs} \epsilon_{rs}. \quad (12)$$

The tensor A_{ijpq} is symmetric and, in Voigt notation, can be represented as a second-order matrix A_{ij} . In the most general case A_{ij} has 21 independent elements. A sixth-order tensor, A_{ijpqrs} , describes nonlinear elastic properties. It is also symmetric and, in Voigt notation, can be represented as a third-order matrix A_{ijk} . In the most general case A_{ijk} has 56 independent elements. Of those elements, six are of the type A_{iii} , 30 are of the type A_{ijj} , and 20 are of the type A_{ijk} ($i \leq j \leq k$).

When the sample is isotropic, A_{ij} has two independent elements (the Lamé parameters), while A_{ijk} has three independent elements (A_{111} , A_{112} , and A_{123}). When the sample has hexagonal symmetry, five independent elements are required to describe A_{ij} and ten elements are required to describe A_{ijk} . Hearmon (1953) gives a complete list of the third-order coefficients for all symmetry classes.

For the sample of Berea Sandstone used in this experiment, we found that A_{ijpq} has hexagonal symmetry. Because Winkler et al. (1998) and Prioul et al. (2001) have shown that isotropic A_{ijpqrs} is sufficient to explain the stress-induced behavior of VTI rocks, and because we have no information to constrain the tensor any further, we assumed isotropic symmetry for the sixth-order tensor A_{ijpqrs} . Using hexagonal symmetry for A_{ijpq} and isotropy for A_{ijpqrs} , we can expand equation (12) as

$$\begin{aligned} C_{1111} &= A_{11} + \tau_{11} + A_{111} \epsilon_{11} + A_{112} (\epsilon_{22} + \epsilon_{33}), \\ C_{2222} &= A_{11} + \tau_{22} + A_{111} \epsilon_{22} + A_{112} (\epsilon_{11} + \epsilon_{33}), \\ C_{3333} &= A_{33} + \tau_{33} + A_{111} \epsilon_{33} + A_{112} (\epsilon_{11} + \epsilon_{22}), \\ C_{1212} &= A_{66} + \tau_{22} + A_{111} \frac{(\epsilon_{11} + \epsilon_{22})}{4} \\ &\quad + A_{112} \left(\frac{\epsilon_{33}}{2} - \frac{(\epsilon_{11} + \epsilon_{22})}{4} \right) - A_{123} \frac{\epsilon_{33}}{2}, \\ C_{1313} &= A_{44} + \tau_{33} + A_{111} \frac{(\epsilon_{11} + \epsilon_{33})}{4} \\ &\quad + A_{112} \left(\frac{\epsilon_{22}}{2} - \frac{(\epsilon_{11} + \epsilon_{33})}{4} \right) - A_{123} \frac{\epsilon_{22}}{2}, \\ C_{2323} &= A_{44} + \tau_{33} + A_{111} \frac{(\epsilon_{22} + \epsilon_{33})}{4} \\ &\quad + A_{112} \left(\frac{\epsilon_{11}}{2} - \frac{(\epsilon_{22} + \epsilon_{33})}{4} \right) - A_{123} \frac{\epsilon_{11}}{2}, \quad (13) \\ C_{2121} &= A_{66} + \tau_{11} + A_{111} \frac{(\epsilon_{11} + \epsilon_{22})}{4} \\ &\quad + A_{112} \left(\frac{\epsilon_{33}}{2} - \frac{(\epsilon_{11} + \epsilon_{22})}{4} \right) - A_{123} \frac{\epsilon_{33}}{2}, \\ C_{3131} &= A_{44} + \tau_{11} + A_{111} \frac{(\epsilon_{11} + \epsilon_{33})}{4} \\ &\quad + A_{112} \left(\frac{\epsilon_{22}}{2} - \frac{(\epsilon_{11} + \epsilon_{33})}{4} \right) - A_{123} \frac{\epsilon_{22}}{2}, \\ C_{3232} &= A_{44} + \tau_{22} + A_{111} \frac{(\epsilon_{22} + \epsilon_{33})}{4} \\ &\quad + A_{112} \left(\frac{\epsilon_{11}}{2} - \frac{(\epsilon_{22} + \epsilon_{33})}{4} \right) - A_{123} \frac{\epsilon_{11}}{2}, \end{aligned}$$

and

$$\begin{aligned} C_{1122} &= A_{12} + A_{112} (\epsilon_{11} + \epsilon_{22}) + A_{123} \epsilon_{33}, \\ C_{1133} &= A_{13} + A_{112} (\epsilon_{11} + \epsilon_{33}) + A_{123} \epsilon_{22}, \quad (14) \\ C_{2233} &= A_{13} + A_{112} (\epsilon_{22} + \epsilon_{33}) + A_{123} \epsilon_{11}. \end{aligned}$$

Table 2. Value for $\epsilon^{(1)}$, $\epsilon^{(2)}$, $\gamma^{(1)}$, $\gamma^{(2)}$, $\delta^{(1)}$, and $\delta^{(2)}$ obtained by methods 1 and 2 at different stress levels. It was impossible to identify pure-shear events in cross-line gathers along the direction of the x_2 -axis, so we did not compute $\gamma^{(1)}$ using method 2.

Stress (MPa)	Method	$\epsilon^{(1)}$	$\epsilon^{(2)}$	$\gamma^{(1)}$	$\gamma^{(2)}$	$\delta^{(1)}$	$\delta^{(2)}$
0	1	0.07 ± 0.02	0.07 ± 0.02	0.09 ± 0.02	0.09 ± 0.02	0.04 ± 0.03	0.04 ± 0.03
0	2	0.05 ± 0.04	0.05 ± 0.04	—	0.08 ± 0.04	0.04 ± 0.03	0.04 ± 0.03
3	1	0.24 ± 0.02	0.03 ± 0.02	0.18 ± 0.02	0.05 ± 0.02	0.15 ± 0.03	0.11 ± 0.03
3	2	0.20 ± 0.04	0.07 ± 0.04	—	0.04 ± 0.04	0.15 ± 0.03	0.11 ± 0.03
6	1	0.35 ± 0.02	0.01 ± 0.02	0.23 ± 0.02	0.05 ± 0.02	0.19 ± 0.03	0.14 ± 0.03
6	2	0.35 ± 0.04	0.10 ± 0.04	—	0.04 ± 0.04	0.19 ± 0.03	0.14 ± 0.03
9	1	0.44 ± 0.02	0.01 ± 0.02	0.29 ± 0.02	0.05 ± 0.02	0.32 ± 0.03	0.16 ± 0.03
9	2	0.31 ± 0.04	0.09 ± 0.04	—	0.05 ± 0.04	0.32 ± 0.03	0.16 ± 0.03

Here, Voigt indices have been used for the symmetric tensors A_{ijpq} and A_{ijpqrs} . The diagonal elements of the tensors A_{ij} and C_{ijpq} are related by equations (13), while the off-diagonal elements of A_{ij} and C_{ijpq} are related by equations (14).

Note that the effective stiffness tensor does not exhibit all of the symmetry properties commonly expected of a stiffness tensor (i.e., $C_{ijpq} \neq C_{jipq}$, $C_{ijpq} \neq C_{ijqp}$, $C_{ijpq} \neq C_{jiqp}$, where $i = p$ and $j = q$). This is an important difference between intrinsic and stress-induced anisotropy. The equations indicate that when uniaxial stress is applied in the isotropy plane $[x_1, x_2]$ of a TI solid, the effective stiffness tensor has a symmetry close to, but not identical to, orthorhombic. The medium differs from orthorhombic because of the asymmetry of the

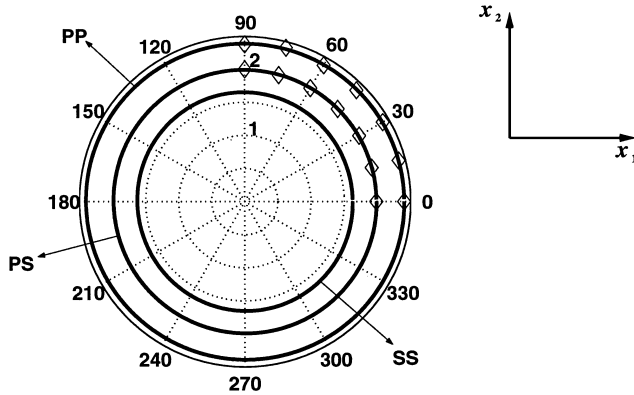


FIG. 8. Polar plots of observed moveout velocities (km/s) of P- and converted PS-waves (diamonds) obtained by semblance analysis for the unstressed state. The best-fit NMO ellipses (solid lines) for P- and PS-modes along with the estimated NMO ellipse for the pure S-mode are also shown. All three ellipses are close to concentric circles, which confirms that $[x_1, x_2]$ (the bedding plane orientation) is the isotropy plane of the unstressed VTI medium.

tensors just mentioned. Consequently, instead of nine independent elements required to describe an orthorhombic medium, the effective stiffness tensor has 12 independent elements [equations (13) and (14)].

COMPARISON OF EXPERIMENTAL RESULTS WITH THE THEORY

Before testing whether experimental results can be explained in terms of nonlinear elasticity, note that in a particular stress state, the diagonal elements of the effective stiffness tensor are related to the velocities \tilde{V}_{Sij} and \tilde{V}_{Pi} of wave modes propagating along the coordinate axes by simple formulas:

$$\begin{aligned} C_{ijij} &= \rho \tilde{V}_{Sij}^2, & (i \neq j) \\ C_{iiii} &= \rho \tilde{V}_{Pi}^2. \end{aligned} \quad (15)$$

Likewise, diagonal elements of the unstressed stiffness tensor are expressed as

$$\begin{aligned} A_{ijij} &= \rho V_{Sij}^2, & (i \neq j) \\ A_{iiii} &= \rho V_{Pi}^2, \end{aligned} \quad (16)$$

where V_{Sij} and V_{Pi} are transmission velocities of S- and P-waves propagating along the coordinate axes measured in the absence of stress. The subscript i refers to the propagation direction, while the subscript j refers to the polarization direction. Thurston (1974) showed that stresses and strains are strictly related via the nonlinear Hooke's law:

$$\epsilon_{ij} = A_{ijpq}^{-1} \tau_{pq} - A_{ijkl}^{-1} A_{lmno}^{-1} A_{pqrs}^{-1} A_{klmors} \tau_{lm} \tau_{pq}. \quad (17)$$

Numerical estimates show that, for the stresses applied, the second (nonlinear) term on the right-hand side is small enough to be ignored. Therefore, to compute strains, we used only the linear part (the first term) of Hooke's law. In computations, we

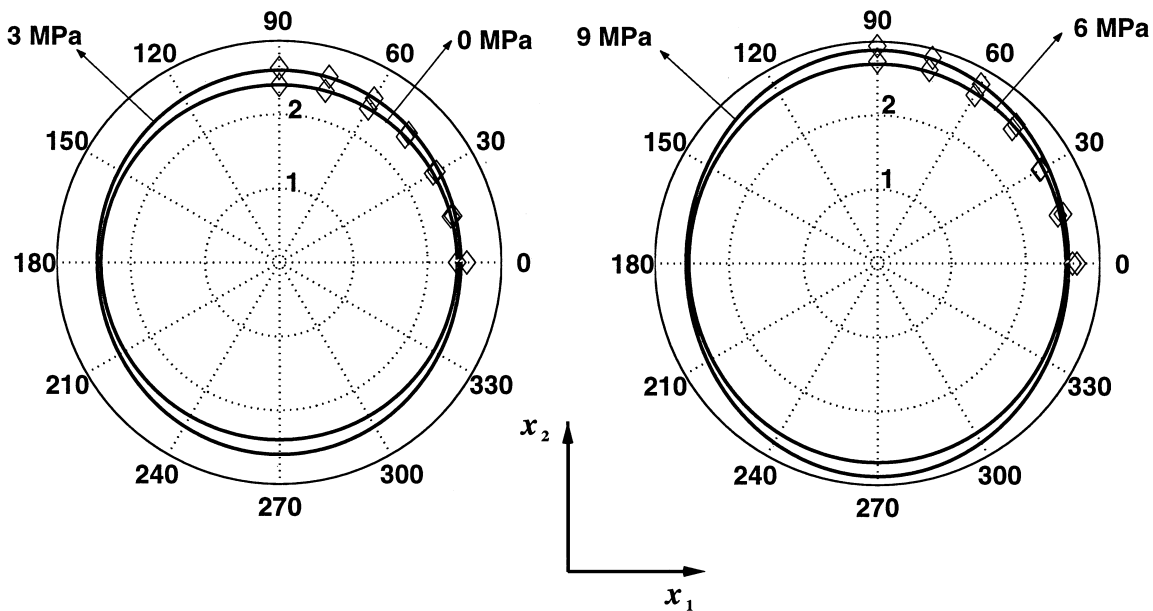


FIG. 9. Polar plots of P-wave moveout velocities (km/s) (diamonds) obtained by semblance analysis at different stress states. The best-fit NMO ellipse (solid lines) for each stress state, assuming that $[x_1, x_3]$ and $[x_2, x_3]$ are symmetry planes of the stressed medium, is also shown. Stress was applied in the x_2 -axis direction (90°).

assumed that the density ρ was equal to 2.14 g/cm^3 for all stress states.

The VTI stiffness tensor (GPa) of Berea Sandstone in the unstressed state was found to be

$$A = \begin{pmatrix} 12.80 \pm 0.20 & -0.44 \pm 0.30 & 0.40 \pm 0.25 & 0 & 0 & 0 \\ -0.44 \pm 0.30 & 12.80 \pm 0.20 & 0.40 \pm 0.25 & 0 & 0 & 0 \\ 0.40 \pm 0.25 & 0.40 \pm 0.25 & 11.30 \pm 0.20 & 0 & 0 & 0 \\ 0 & 0 & 0 & 5.68 \pm 0.20 & 0 & 0 \\ 0 & 0 & 0 & 0 & 5.68 \pm 0.20 & 0 \\ 0 & 0 & 0 & 0 & 0 & 6.62 \pm 0.20 \end{pmatrix}.$$

We computed the diagonal elements using equations (16) and estimated the off-diagonal element $A_{13} = A_{23}$ from the parameter δ using an equation similar to equation (A-5) or (A-8). We derived Thomsen's parameter δ from P-wave NMO and vertical velocities [equation (4)] and obtained the other off-diagonal element, A_{12} , from $A_{12} = A_{11} - 2A_{66}$. The error bars were computed by propagating the error in transmission velocities ($\pm 0.02 \text{ km/s}$) and NMO velocities ($\pm 0.05 \text{ km/s}$) in equations (15) and (16).

Evaluation of third-order coefficients

Knowing the diagonal elements of the stiffness tensors and the strains, we computed the third-order coefficients using a linear least-squares inversion of equation (13). We repeated the procedure for each uniaxial stress state ($\tau_{22} = -3 \text{ MPa}$; $\tau_{22} = -6 \text{ MPa}$; $\tau_{22} = -9 \text{ MPa}$) to estimate three sets of third-order tensors: $A_{ijk}^{(0-3)}$, $A_{ijk}^{(0-6)}$, $A_{ijk}^{(0-9)}$. The numeric superscript indicates

the two stress levels involved in the least-squares procedure. We found that $A_{111}^{(0-3)} = -15\,357$, $A_{112}^{(0-3)} = 1344$, $A_{123}^{(0-3)} = 313$; $A_{111}^{(0-6)} = -14\,231$, $A_{112}^{(0-6)} = 398$, $A_{123}^{(0-6)} = 906$; and $A_{111}^{(0-9)} = -12\,126$, $A_{112}^{(0-9)} = -143$, $A_{123}^{(0-9)} = 225$, all in GPa units.

The mean (μ_k) of the three estimates for each A_{ijk} is shown in Table 3 along with its standard deviation (δ_k), which is somewhat indicative of the error in the estimate. Also shown in Table 3 are other previously published measurements of the third-order tensor for Berea Sandstone. The standard deviation is defined here as

$$\sqrt{\frac{\sum_{i=1}^n (d_{ik} - \mu_k)^2}{n - 1}},$$

where $n = 3$, and the quantity d_{ik} refers to an independent element of the third-order stiffness tensor computed using a particular stress level. The index $i = 1, 2, 3$ denotes the stress state, and the index $k = 1, 2, 3$ denotes an element of the third-order stiffness tensor.

Predicting transmission velocities

Using each estimate of the third-order tensor— $A_{ijk}^{(0-3)}$, $A_{ijk}^{(0-6)}$, and $A_{ijk}^{(0-9)}$ —we predicted the diagonal elements of the effective stiffness tensor at all stress levels and then computed velocities from the predicted diagonal elements as $\tilde{V}_{Sij} = \sqrt{C_{ijij}}/\rho$ (S-waves, where $i \neq j$) and $\tilde{V}_{Pi} = \sqrt{C_{iiii}}/\rho$ (P-waves). Therefore, at each stress level we made three predictions for each wave mode. Note that two of the three predictions (made for each wave mode at each stress level) were computed using third-order tensors estimated from velocities observed at stress levels other than the one being studied. The mean of the predicted values is plotted in Figure 11 as a function of the applied stress. The standard deviation of each predicted quantity is equal to half the length of the error bar. The error bars of $\pm 0.02 \text{ km/s}$ for the measured velocities are smaller than the size of the symbols used and are not plotted.

Figure 11a compares the measured and predicted P-wave velocities. In accordance with the VTI symmetry, V_{P1} and V_{P2} are equal in the unstressed state. With increasing stress level, V_{P2} increases with stress, while V_{P1} and V_{P3} remain virtually unchanged. This behavior is well predicted by nonlinear elasticity theory; however, the theory predicts V_{P3} to be slightly more sensitive than V_{P1} to the stress level, while the data show just the opposite.

Figure 11b shows S-wave velocities V_{S23} and V_{S13} , and Figure 11c shows S-wave velocities V_{S32} and V_{S31} . In accordance

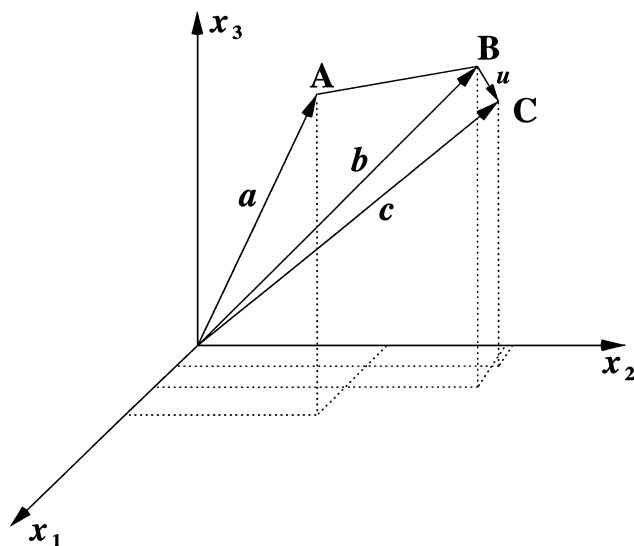


FIG. 10. Schematic diagram depicting the position of an arbitrary particle in the unstressed state **A**, the stressed state **B**, and the wave-propagation state **C**. Letters **a**, **b** and **c** are position vectors of a particle for states **A**, **B**, and **C**, respectively, **u** denotes the displacement vector resulting from a small amplitude disturbance.

with VTI symmetry, V_{S23} , V_{S13} , V_{S32} , and V_{S31} are equal in the unstressed state. As the stress level increases, note that the velocities of S-waves propagating in the direction of the applied stress or polarized in the direction of the applied stress increase, while the velocities of S-waves propagating in a direction perpendicular to the applied stress and polarized perpendicular to the applied stress are virtually unchanged. This behavior is well predicted by the theory.

Figure 11d shows S-wave velocities V_{S12} and V_{S21} . For an orthorhombic solid, V_{S12} should be equal to V_{S21} ; however, for stress-induced anisotropy they may be different [equations (13)]. The nonlinear theory predicts negligible asymmetry ($C_{1212} - C_{2121} = \tau_{22} - \tau_{11} \approx$ a few MPa), but the observed asymmetry is significantly larger. This large asymmetry is not unique to Berea Sandstone or to our experimental setup. It was also observed in shales by Hornby (1998) and in Colton Sandstone by Dillen et al. (1999). We do not have an explanation for this phenomenon, but we believe this is an important observation that deserves further study. In spite of this discrepancy, the theory correctly predicts our observations that $C_{1212} \neq C_{2121}$ and $C_{2323} \neq C_{3232}$, while $C_{1313} = C_{3131}$.

Note on the use of the Tsvankin (orthorhombic) parameters

The theory predicts that a uniaxial stress applied in the isotropy plane of a TI rock results in an effective stiffness tensor with symmetry close to, but not truly, orthorhombic [equations (13)-(14)]. The stiffness tensor of an intrinsically orthorhombic medium differs from the effective stiffness tensor of a stress-induced orthorhombic medium by virtue of the asymmetry in the latter. Theoretical predictions suggest that the asymmetry should be negligible and can be ignored (see Figure 11 for predicted velocities), but our observed data show considerable asymmetry. Therefore, the anisotropic parameters defined for a symmetric orthorhombic tensor [equations (A-2)–(A-10), Tsvankin (1997)] are not strictly applicable to our data.

In principle, however, Tsvankin's parameters can be generalized for asymmetric tensors of a stress-induced medium. Although such a parameterization requires three additional parameters to account for the asymmetry of the shear modes, the parameterization is attractive because it provides a simple description of conventional seismic signatures (e.g., NMO velocities). In this study, we do not attempt to generalize Tsvankin's parameters for asymmetric tensors but have opted instead for a simple adaptation of those parameters as shown in the appendix [equations (A-11)–(A-12)].

Theoretical anisotropic parameters in the weak anisotropy limit

Before comparing experimental and predicted anisotropic parameters derived from the velocities, it is important to establish the analytic relationships between Tsvankin's parameters that control seismic signatures and the stress magnitudes. The exact expressions for Tsvankin's parameters in terms of stresses, however, are too complicated. From such relationships, it is also difficult to gain any insight into the influence of stress magnitude on the effective anisotropic model. Therefore, we apply a weak anisotropy approximation (Bakulin et al., 2000a,b) and assume that both intrinsic anisotropy and stress-induced changes act as small perturbations imposed on some isotropic unstressed reference background.

Each element of the stiffness tensor in equations (13)-(14) can be represented as

$$C_{ijpq} = A_{ij}(1 + \Delta_{ijpq}), \quad (18)$$

where Δ_{ijpq} is a dimensionless perturbation introduced by the stress and the Einstein summation is not implied. The weak

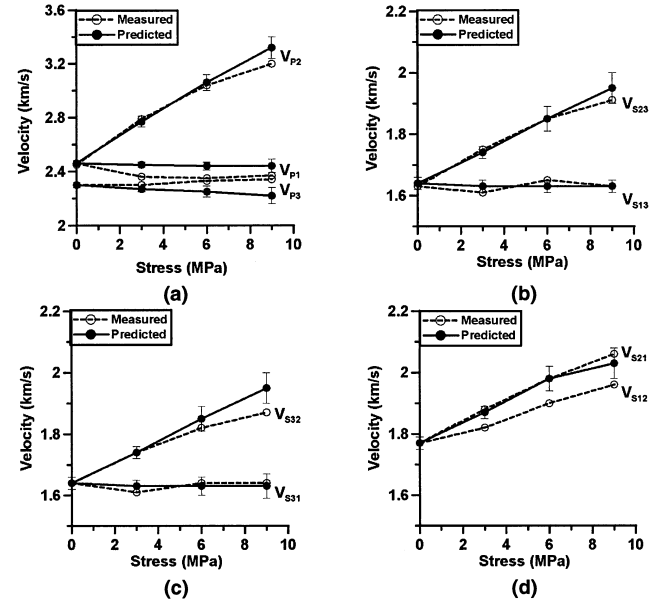


FIG. 11. Measured and predicted P- and S-wave velocities along the axes directions as functions of the applied stress. The stress was applied in the direction of the x_2 -axis. (a) P-waves propagating along the three coordinate axes, (b) S-waves polarized along the x_3 -axis, (c) S-waves propagating along the x_3 -axis, (d) S-waves in the $[x_1-x_2]$ -plane.

Table 3. Estimated third-order coefficients A_{ijk} and unstressed elastic properties [V_P , V_S (measured perpendicular to bedding), ρ] for Berea Sandstone.

Source	ρ (kg/m ³)	V_P (m/s)	V_S (m/s)	A_{111} (GPa)	A_{112} (GPa)	A_{123} (GPa)	V_S/V_P
Winkler et al., 1998	2062	1900	1350	-12 884	-2546	1269	0.71
Winkler et al., 1998	2062	2127	1418	-9550	-1370	1062	0.67
Winkler and Liu, 1996	2120	2183	1457	-17 038	-3272	-3160	0.67
Winkler and Liu, 1996	2080	2037	1334	-29 106	-6940	-2090	0.65
Sinha and Kostek, 1996	2062	2320	1500	-21 217	-8044	2361	0.65
Present study (mean value)	2140	2300	1640	$-13\,904 \pm 1944$	533 ± 699	481 ± 370	0.71

anisotropy assumption means that all Δ_{ijpq} , along with the unstressed background parameters ϵ_b , δ_b , and γ_b are small quantities of the same order. Expressing equation (18) in terms of the linearized anisotropic parameters yields

$$\epsilon^{(1)} = \epsilon_b + \frac{K_p}{2A_{55}}(\tau_{22} - \tau_{33}), \quad \epsilon^{(2)} = \epsilon_b + \frac{K_p}{2A_{55}}(\tau_{11} - \tau_{33}), \quad (19)$$

$$\delta^{(2)} = \delta_b + \frac{K_p}{2A_{55}}(\tau_{22} - \tau_{33}), \quad \delta^{(1)} = \delta_b + \frac{K_p}{2A_{55}}(\tau_{11} - \tau_{33}), \quad (20)$$

$$\gamma^{(1)} = \gamma_b + \frac{K_s}{2A_{55}}(\tau_{22} - \tau_{33}), \quad \gamma^{(2)} = \gamma_b + \frac{K_s}{2A_{55}}(\tau_{11} - \tau_{33}), \quad (21)$$

$$\delta^{(3)} = \frac{K_p}{2A_{55}}(\tau_{22} - \tau_{11}), \quad (22)$$

where

$$K_p = \frac{2A_{155}}{A_{33}}, \quad K_s = \frac{A_{456}}{A_{55}}, \quad (23)$$

and where $A_{155} = (A_{111} - A_{112})/4$, $A_{456} = (A_{111} - 3A_{112} + 2A_{123})/8$ are two combinations of the three third-order elastic constants that control the stress-induced part of the P- and S-wave anisotropy, respectively. Note that small terms in equations (13) represented by τ_{ii} (responsible for asymmetry of the stiffness tensor) are ignored in this approximation.

Each anisotropic parameter consists of two distinct parts: one resulting from the background intrinsic anisotropy of the unstressed rock and the other from the stress. This is a consequence of the weak anisotropy addition rule noted by Bakulin et al. (2000b) while analyzing a combination of intrinsic and fracture-induced anisotropy. Intrinsic anisotropy is represented by the Thomsen parameters ϵ_b , δ_b , and γ_b of the unstressed rock. The parameter $\delta^{(3)}$ does not contain background anisotropic parameters because $[x_1, x_2]$ is the isotropy plane of the unstressed VTI medium. The stress-induced part of the anisotropy (from here on denoted by subscript $s-i$) is expressed by equations (19)–(22), with $\epsilon_b = \delta_b = \gamma_b = 0$. It is characterized by elliptical anisotropy in all three symmetry planes, which in Tsvankin's notation is expressed as

$$\epsilon_{s-i}^{(1)} = \delta_{s-i}^{(1)}, \quad \epsilon_{s-i}^{(2)} = \delta_{s-i}^{(2)}, \quad \delta_{s-i}^{(3)} = \epsilon_{s-i}^{(1)}, \quad -\epsilon_{s-i}^{(2)}. \quad (24)$$

This agrees with Rasolofosaon (1998), who noted that isotropic materials subjected to an arbitrary triaxial stress field become, effectively, an orthorhombic medium with elliptical anisotropy in each symmetry plane. Certain specific models for granular and cracked media also predict elliptical VTI anisotropy under uniaxial stress (Schwartz et al., 1994).

For uniaxial stress $\tau_{11} = \tau_{33} = 0$, $\tau_{22} \neq 0$, equations (19)–(21) may be further simplified to

$$\epsilon^{(1)} = \epsilon_b + \frac{K_p}{2A_{55}}\tau_{22}, \quad \epsilon^{(2)} = \epsilon_b, \quad (25)$$

$$\delta^{(1)} = \delta_b + \frac{K_p}{2A_{55}}\tau_{22}, \quad \delta^{(2)} = \delta_b, \quad (26)$$

$$\gamma^{(1)} = \gamma_b + \frac{K_s}{2A_{55}}\tau_{22}, \quad \gamma^{(2)} = \gamma_b. \quad (27)$$

Therefore, we expect that anisotropic parameters in the symmetry plane $[x_1, x_3]$ normal to the applied stress should stay

close to the Thomsen parameters of the unstressed rock. In the vertical plane containing the applied stress direction, $[x_2, x_3]$, we expect each anisotropic parameter to increase linearly with the stress magnitude. The stress-induced part of the anisotropic parameters should be positive because the values of $K_p = -637$, $K_s = -319$, and uniaxial stress τ_{22} are negative in accordance with our convention on compressive stresses.

Numerical comparison of anisotropic parameters

Although the weak anisotropy approximations provide useful insight into the interdependence between anisotropy and stress, we use the exact equations and A_{ijk} found from the data to predict the anisotropic parameters $\epsilon^{(i)}$, $\delta^{(i)}$, and $\gamma^{(i)}$ under stress and then compare them with the experimental values obtained by method 1 (Table 2).

The predicted effective stiffness tensor for our sample of Berea Sandstone was computed using equations (13)–(14). Since the difference between the predicted values of C_{ijij} and C_{jiji} was negligible, we ignored the asymmetry and computed the anisotropic parameters from equations (A-4)–(A-10).

Figure 12 shows the variation of the ϵ , γ , and δ parameters with stress. In accordance with the weak anisotropy

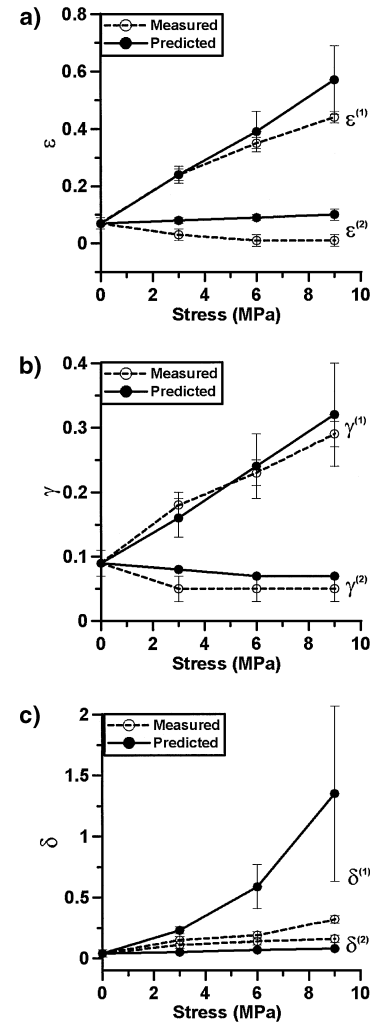


FIG. 12. Measured and predicted (a) $\epsilon^{(1)}$ and $\epsilon^{(2)}$ versus stress, (b) $\gamma^{(1)}$ and $\gamma^{(2)}$ versus stress, and (c) $\delta^{(1)}$ and $\delta^{(2)}$ versus stress applied in the x_2 -direction.

approximation [equations (25)–(27)], both the predicted and measured anisotropic parameters $\epsilon^{(2)}$, $\delta^{(2)}$, and $\gamma^{(2)}$, defined in the vertical plane normal to the applied stress $[x_1, x_3]$, are almost insensitive to stress. In contrast, the anisotropic parameters $\epsilon^{(1)}$, $\delta^{(1)}$, and $\gamma^{(1)}$, defined in the vertical plane $[x_2, x_3]$ containing the stress direction all increase in a nearly linear fashion. As is predicted by equations (25)–(27), the deviation from the linear dependence is evident only at the higher levels of stress, where anisotropy is strong.

In general, except for the parameter $\delta^{(1)}$ (Figure 12c), we observe satisfactory agreement between all measured and predicted anisotropic parameters. Several possible reasons that may contribute to the poor match in $\delta^{(1)}$ are outlined in the discussion section. We also note that the predicted values of $\delta^{(1)}$ are extremely large. Tsvankin (2001) determined that the parameter δ for VTI media is bounded by $-0.5 \leq \delta \leq 2$; however, he assumed that the minimum value of $V_{P0}/V_{S0} = \sqrt{2} \approx 1.41$. In our experiment the corresponding ratio, V_{P3}/V_{S32} in the $[x_2, x_3]$ -plane, is as small as 1.25 for a stress of 9 MPa (see Table 1), which increases the upper bound of $\delta^{(1)}$ to 3.55.

DISCUSSION

Differences between the predicted and observed velocities and anisotropic parameters may arise as a result of hysteresis, substantial magnitude of deformation, an anisotropic third-order stiffness tensor, and heterogeneous distribution of stress in the sample. We believe our measurements of distances between sources and receivers are accurate, and any error caused by the deformation in the sample is negligible and can be ignored.

Hysteresis.—Table 4 shows the transmission velocities measured along the coordinate axes at zero uniaxial stress before the application of each new stress state. Note that the rock does not return to its original state after being subjected to uniaxial stress. We speculate that the observed hysteresis is the result of a change in crack distribution caused by the presence of the initial stress field.

Hooke's law and deformation gradients.—No strain gauges were placed in or on the rock; therefore, we are unable to use actual measurements of strains and deformation gradients. Our analysis presented was possible only because the estimated strains are small ($\approx 10^{-4}$). When strains are large, the nonlinear (second) term is required in Hooke's law [equation (17)], and the deformation gradient tensor can no longer be approximated with the Kronecker delta function. Future experiments should use strain gauges so rock deformation can be monitored accurately.

Sixth-order tensors.—Use of an isotropic sixth-order tensor was an important assumption in this study. In the absence

of any knowledge about the symmetry of the sixth-order tensor, isotropy offered the simplest possible parameterization. Also, an isotropic sixth-order tensor is often sufficient to explain the stress-induced effective stiffness tensor of unstressed VTI rocks (Prioul et al., 2001). The VTI sixth-order tensor requires ten independent elements and, in general, is difficult to estimate in practice. Future work may attempt to invert for a larger number (between three and ten) of VTI sixth-order constants and try to improve the match between predicted and measured elastic properties of anisotropic rocks under stress. Although using the correct symmetry of the sixth-order stiffness tensor can improve the accuracy of the predictions, it does not influence the asymmetry of the effective stress-induced stiffness tensor. Theory predicts that the asymmetry is determined solely by the applied stress tensor [equation (11)].

Homogeneous stress distribution.—In studies related to stress-induced anisotropy, it is common to assume that the stress distribution in the sample is uniform, but rarely is this assumption ever put to the test. In our study, we too make such an assumption but do not attempt to monitor the stress distribution at different stress states. Therefore, the possibility of having a nonuniform stress distribution in our experiments exists. One way to detect stress concentration in the sample is to record transmission velocities along the x_3 -axis at different points in the $[x_1, x_2]$ plane at each stress state. If indeed the stresses are constant over the sample, velocities along the x_3 -axis will not vary with position in the $[x_1, x_2]$ plane. However, if stress concentrations are present, velocities along the x_3 -axis will be position dependent. We advise following some such procedure in future experiments.

CONCLUSIONS

Despite many existing and potential challenges, our study offers an approach for estimating the orientation and magnitudes of subsurface principal stresses using seismic data. First, 3D seismic measurements could be used to establish directions of the principal stresses, which correspond to the principal axes of the effective orthorhombic medium. Then, using methods described in this paper, the Tsvankin parameters $\epsilon^{(1,2)}$, $\delta^{(1,2)}$, and $\gamma^{(1,2)}$ could be estimated. In practice, these parameters could also be estimated from amplitude variation with offset and azimuth (Rüger, 1998) and multiazimuth vertical seismic profiling (Bakulin et al., 2000c). Using third-order constants estimated from laboratory measurements (Bakulin et al., 2000d; Winkler and Liu, 1996) or borehole acoustic measurements (Sinha, 2001; Sinha and Winkler, 1999), one might relate the estimated Tsvankin's parameters to the stress levels.

To gain a better understanding of the influence of stress on the effective medium, we simplified the anisotropic parameters under the assumption of weak background and stress-induced

Table 4. Velocities in the unstressed state measured at different stages of the experiment. Velocities V_{S32} and V_{S31} were not measured at the unstressed state after 6 MPa.

	V_{P1} (km/s)	V_{P2} (km/s)	V_{P3} (km/s)	V_{S23} (km/s)	V_{S13} (km/s)	V_{S12} (km/s)	V_{S32} (km/s)	V_{S31} (km/s)	V_{S21} (km/s)
Initial	2.45 ± 0.02	2.45 ± 0.02	2.30 ± 0.02	1.63 ± 0.02	1.63 ± 0.02	176 ± 0.02	1.62 ± 0.02	1.62 ± 0.02	1.76 ± 0.02
After 3 MPa	2.41 ± 0.02	2.45 ± 0.02	2.31 ± 0.02	1.63 ± 0.02	1.63 ± 0.02	1.77 ± 0.02	1.60 ± 0.02	1.59 ± 0.02	1.75 ± 0.02
After 6 MPa	2.32 ± 0.02	2.39 ± 0.02	2.20 ± 0.02	1.61 ± 0.02	1.58 ± 0.02	1.71 ± 0.02			1.71 ± 0.02

anisotropy. We found that each anisotropic parameter is the sum of the corresponding Thomsen parameter of the VTI unstressed medium and a stress-related contribution. The part attributable to stress is proportional to the difference between the principal stresses acting in a symmetry plane corresponding to the anisotropic parameter under examination. Therefore, if two principal stresses in a symmetry plane are equal, the stress-related term vanishes. For hydrostatic stress ($\tau_{11} = \tau_{22} = \tau_{33}$) the anisotropic parameters of the stressed and unstressed media should be equal. We also confirmed Rasolofosaon's result that the stress-induced part of the anisotropic parameters has an elliptical form in all symmetry planes. Therefore, $\epsilon_{s-i}^{(1)} = \delta_{s-i}^{(1)}$, $\epsilon_{s-i}^{(2)} = \delta_{s-i}^{(2)}$ and $\delta_{s-i}^{(3)} = \epsilon_{s-i}^{(1)} - \epsilon_{s-i}^{(2)}$, where $s - i$ denotes the stress-induced part in equations (19)–(22). These constraints differ from the ones existing for fracture-induced anisotropy (Bakulin et al., 2000a,b) and can be used in practice to distinguish between fracture-induced and stress-induced anisotropy.

Nonlinear elasticity may have application in a wide range of problems related to estimating 3D stress and pore pressure in anisotropic formations. Perhaps our results will motivate more field and laboratory experiments related to anisotropic rocks under complex subsurface stress conditions.

ACKNOWLEDGMENTS

We thank Vladimir Grechka [formerly Colorado School of Mines (CSM), presently Shell] and Ilya Tsvankin (CSM) for their help and advice throughout this study. We also thank Schlumberger for permission to publish this paper, Claude Signer and Michael Thambynayagam (Schlumberger) for supporting this study, and the Mining Department of the Colorado School of Mines for allowing us to use its MTS system. We appreciate reviews of the manuscript by Ken Larner and Ilya Tsvankin (CSM), and Wayne Pennington (Michigan Technological University). Many insightful suggestions by Geophysics reviewers Jim Brown, Dan Ebrom, and Bikash Sinha helped improve this manuscript. D. S. thanks the industry sponsors of the Center for Wave Phenomena at CSM for financial support.

REFERENCES

- Bakulin, A. V., Grechka, V., and Tsvankin, I., 2000a, Estimation of fracture parameters from reflection seismic data, part I: HTI model due to a single fracture set: *Geophysics*, **65**, 1788–1802.
- , 2000b, Estimation of fracture parameters from reflection seismic data, part II: Fractured models with orthorhombic symmetry: *Geophysics*, **65**, 1803–1817.
- Bakulin, A., Slater, C., Bunain, H., and Grechka, V., 2000c, Estimation of azimuthal anisotropy and fracture parameters from multi-azimuthal walkaway VSP in the presence of lateral heterogeneity: 70th Ann. Internat. Mtg., Soc. Expl. Geophys., Expanded Abstracts, 1405–1408.
- Bakulin, A. V., Troyan, V. N., and Bakulin, V. N., 2000d, Acoustoelasticity of rocks: St. Petersburg Univ. Press (in Russian).
- Bourgoyne, Jr., A. T., Milheim, K. K., Chenevert, M. E., and Young, F. S., 1991, Applied drilling engineering: Soc. Petr. Eng., 286–287.
- Bowers, G. L., 1995, Pore pressure estimation from velocity data: Accounting for overpressure mechanisms besides undercompaction: *SPE Drill. and Compl.*, **10**, 89–95.
- Dillen, M. W. P., Cruts, H. M. A., Groenenboom, J., Fokkema, J. T., and Duijndam, A. J. W., 1999, Ultrasonic velocity and shear-wave splitting behavior of a Colton sandstone under a changing triaxial stress: *Geophysics*, **64**, 1603–1607.
- Eaton, B. A., 1975, The equation for geopressure prediction from well logs: Soc. Petr. Eng. Publ. 5544, 1–11.
- Fjær, E., Holt, R., Horsrud, P., and Raaen, I., 1992, Petroleum related rock mechanics: Elsevier Science Publ. Co., Inc.
- Grechka, V., Theophanis, S., and Tsvankin, I., 1999, Joint inversion of P- and PS-waves in orthorhombic media: Theory and a physical modeling study: *Geophysics*, **64**, 146–161.
- Grechka, V., Tsvankin, I., Bakulin, A., Hansen, J. O., and Signer, C., 2002, Joint inversion of PP and PS reflection data for VTI media: A North Sea case study: *Geophysics*, **67**, 1382–1395.
- Hearmon, R. F. S., 1953, 'Third-order' elastic coefficients: *Acta Cryst.*, **6**, 331–340.
- Hornby, B. E., 1998, Experimental laboratory determination of the dynamic elastic properties of wet, drained shales: *J. Geophys. Res.*, **103**, 945–964.
- Johnson, P. A., and Rasolofosaon, P. N. J., 1996, Nonlinear elasticity and stress-induced anisotropy in rock: *J. Geophys. Res.*, **101**, 3113–3124.
- Lo, T. W., Coyner, K. B., and Toksoz, M. N., 1986, Experimental determination of elastic anisotropy of Berea Sandstone, Chicopee Shale, and Chelmsford Granite: *Geophysics*, **51**, 164–171.
- Mavko, G., Mukerji, T., and Godfrey, N., 1995, Predicting stress-induced velocity anisotropy in rocks: *Geophysics*, **60**, 1222–1233.
- Nur, A., 1971, Effects of stress on velocity anisotropy in rocks with cracks: *J. Geophys. Res.*, **76**, 2022–2034.
- Prasad, M., and Manghnani, M. H., 1997, Effects of pore and differential pressure on compressional wave velocity and quality factor in Berea and Michigan sandstones: *Geophysics*, **62**, 1163–1176.
- Prioul, R., Bakulin, A., and Bakulin, V., 2001, Three-parameter model for predicting acoustic velocities in transversely isotropic rocks under arbitrary stress: 71st Ann. Internat. Mtg., Soc. Expl. Geophys., Expanded Abstracts, 1732–1735.
- Rasolofosaon, P., 1998, Stress-induced seismic anisotropy revisited: *Revue de l'Institut Français du Pétrole*, **53**, 679–693.
- Rüger, A., 1998, Variation of P-wave reflectivity with offset and azimuth in anisotropic media: *Geophysics*, **63**, 935–947.
- Schwartz, L. M., Murphy, III, W. F., and Berryman, J. G., 1994, Stress-induced transverse isotropy in rocks: 64th Ann. Internat. Mtg., Soc. Expl. Geophys., Expanded Abstracts, 1081–1085.
- Sinha, B. K., 2001, Stress-induced changes in the borehole Stoneley and flexural dispersions: 71st Ann. Internat. Mtg., Soc. Expl. Geophys., Expanded Abstracts, 337–340.
- Sinha, B. K., and Kostek, S., 1996, Stress-induced azimuthal anisotropy in borehole flexural waves: *Geophysics*, **61**, 1899–1907.
- Sinha, B. K., and Winkler, K. W., 1999, Formation nonlinear constants from sonic measurements at two borehole pressures: *Geophysics*, **64**, 1890–1900.
- Sinha, B. K., Kane, M. R., and Frignet, B., 2000, Dipole dispersion crossover and sonic logs in a limestone reservoir: *Geophysics*, **65**, 390–407.
- Taner, M. T., and Koehler, T., 1969, Velocity spectra: Digital computer derivation and applications of velocity functions: *Geophysics*, **34**, 859–881.
- Thomsen, L., 1986, Weak elastic anisotropy: *Geophysics*, **51**, 1954–1966.
- Thurston, R. N., 1974, Waves in solids, in Flügge, S., Ed., *Mechanics of solids*, in Truesdell, C., Ed., *Encyclopedia of physics* **V1a/4**, Springer-Verlag Berlin, 109–308.
- Thurston, R. N., and Brugger, K., 1964, Third-order elastic constants and the velocity of small amplitude elastic waves in homogeneously stressed media: *Phys. Rev. A*, **133**, 1604–1610.
- Tsvankin, I., 1997, Anisotropic parameters and P-wave velocity for orthorhombic media: *Geophysics*, **62**, 1292–1309.
- , 2001, Seismic signatures and analysis of reflection data in anisotropic media: Elsevier Science Publ. Co., Inc.
- Winkler, K. W., and Liu, X., 1996, Measurements of third-order elastic constants in rocks: *J. Acoust. Soc. Am.*, **100**, 1392–1398.
- Winkler, K. W., Sinha, B. K., and Plona, T. J., 1998, Effects of borehole stress concentrations of dipole anisotropy measurements: *Geophysics*, **63**, 11–17.

APPENDIX

ANISOTROPIC PARAMETERS FOR ORTHORHOMBIC MEDIA

Elastic properties of orthorhombic solids are conventionally represented in condensed (Voigt) notation by the stiffness matrix with nine independent elements:

$$\mathbf{C} = \begin{pmatrix} C_{11} & C_{12} & C_{13} & 0 & 0 & 0 \\ C_{12} & C_{22} & C_{23} & 0 & 0 & 0 \\ C_{13} & C_{23} & C_{33} & 0 & 0 & 0 \\ 0 & 0 & 0 & C_{44} & 0 & 0 \\ 0 & 0 & 0 & 0 & C_{55} & 0 \\ 0 & 0 & 0 & 0 & 0 & C_{66} \end{pmatrix}. \quad (\text{A-1})$$

In describing seismic signatures (e.g., NMO velocities and amplitude versus offset gradients), the elements of this stiffness tensor have proved to be inconvenient. A more efficient parameterization to describe seismic signatures, given by Tsvankin (1997), is defined below.

The P -wave vertical velocity; V_{P0} , is

$$V_{P0} \equiv \sqrt{\frac{C_{33}}{\rho}}. \quad (\text{A-2})$$

The vertical velocity of the S -wave polarized in the x_1 -direction, V_{S0} , is

$$V_{S0} \equiv \sqrt{\frac{C_{55}}{\rho}}. \quad (\text{A-3})$$

The VTI parameters ϵ , δ , and γ in the $[x_1, x_3]$ symmetry plane normal to the x_2 -axis (this explains the superscript 2) or $\epsilon^{(2)}$, $\delta^{(2)}$, and $\gamma^{(2)}$, are

$$\epsilon^{(2)} \equiv \frac{C_{11} - C_{33}}{2C_{33}}, \quad (\text{A-4})$$

$$\delta^{(2)} \equiv \frac{(C_{13} + C_{55})^2 - (C_{33} - C_{55})^2}{2C_{33}(C_{33} - C_{55})}, \quad (\text{A-5})$$

$$\gamma^{(2)} \equiv \frac{C_{66} - C_{44}}{2C_{44}}. \quad (\text{A-6})$$

The VTI parameters ϵ , δ , and γ in the $[x_2, x_3]$ symmetry plane, $\epsilon^{(1)}$, $\delta^{(1)}$, and $\gamma^{(1)}$, are

$$\epsilon^{(1)} \equiv \frac{C_{22} - C_{33}}{2C_{33}}, \quad (\text{A-7})$$

$$\delta^{(1)} \equiv \frac{(C_{23} + C_{44})^2 - (C_{33} - C_{44})^2}{2C_{33}(C_{33} - C_{44})}, \quad (\text{A-8})$$

$$\gamma^{(1)} \equiv \frac{C_{66} - C_{55}}{2C_{55}}. \quad (\text{A-9})$$

The VTI parameter δ in the $[x_1, x_2]$ plane (x_1 plays the role of the symmetry axis), or $\delta^{(3)}$, is

$$\delta^{(3)} \equiv \frac{(C_{12} + C_{66})^2 - (C_{11} - C_{66})^2}{2C_{11}(C_{11} - C_{66})}. \quad (\text{A-10})$$

These nine parameters fully describe wave propagation in general orthorhombic media with a known orientation of the symmetry planes. For VTI media, $\epsilon^{(1)} = \epsilon^{(2)}$, $\delta^{(1)} = \delta^{(2)}$, $\gamma^{(1)} = \gamma^{(2)}$, and $\delta^{(3)} = 0$. Therefore, only five parameters are required to describe the VTI medium.

For stressed media, shear velocities V_{Sij} (for propagation along the x_i -axis and polarization along the x_j -axis) and V_{Sji} (for propagation along the x_j -axis and polarization along the x_i -axis) are unequal, resulting in an asymmetric stiffness tensor ($C_{ijpq} \neq C_{jipq}$, $C_{ijpq} \neq C_{ijqp}$, $C_{ijpq} \neq C_{jiqp}$). For an asymmetric stiffness tensor, we adopted the following approximations to Tsvankin parameters. For anisotropic parameters in the $[x_1, x_3]$ plane,

$$\begin{aligned} \epsilon^{(2)} &\equiv \frac{C_{1111} - C_{3333}}{2C_{3333}}, \\ \delta^{(2)} &\equiv \frac{(C_{1133} + C_{3131})^2 - (C_{3333} - C_{3131})^2}{2C_{3333}(C_{3333} - C_{3131})}, \\ \gamma^{(2)} &\equiv \frac{C_{1212} - C_{3232}}{2C_{3232}}. \end{aligned} \quad (\text{A-11})$$

For anisotropic parameters in the $[x_2, x_3]$ plane,

$$\begin{aligned} \epsilon^{(1)} &\equiv \frac{C_{2222} - C_{3333}}{2C_{3333}}, \\ \delta^{(1)} &\equiv \frac{(C_{2233} + C_{3232})^2 - (C_{3333} - C_{3232})^2}{2C_{3333}(C_{3333} - C_{3232})}, \\ \gamma^{(1)} &\equiv \frac{C_{2121} - C_{3131}}{2C_{3131}}. \end{aligned} \quad (\text{A-12})$$

Since the asymmetry of the predicted stiffness tensor is negligible, replacing C_{ijij} with C_{jiji} will not change the results significantly. Our choice to use C_{ijij} rather than C_{jiji} in equations (A-11) and (A-12) was arbitrary.

Errata

To: “Anisotropic inversion of seismic data for stressed media: Theory and a physical modeling study on Berea Sandstone” (D. Sarkar, A. Bakulin, and R. L. Kranz, *Geophysics*, 68, 690–704).

In equation (20) $\delta^{(2)}$ should be replaced by $\delta^{(1)}$, and $\delta^{(1)}$ should be replaced by $\delta^{(2)}$. The correct equation follows.

$$\delta^{(1)} = \delta_b + \frac{K_p}{2A_{55}}(\tau_{22} - \tau_{33}), \quad \delta^{(2)} = \delta_b + \frac{K_p}{2A_{55}}(\tau_{11} - \tau_{33}). \quad (20)$$